Title: Acrobatics at the insect-scale: a durable, precise, and agile micro-aerial-robot

Authors:

Suhan Kim[1]†, Yi-Hsuan Hsiao[1]†, Zhijian Ren[1], Jiashu Huang[1,2], Yufeng Chen[1]*

Affiliations:

[1]Department of Electrical Engineering and Computer Science, Massachusetts Institute of Technology, 77 Massachusetts Avenue, Cambridge, MA, 02139, USA

[2]Department of Physics, Brown University, 69 Brown Street, Providence, RI, 02912, USA

*Corresponding author. Email: yufengc@mit.edu

†These authors contributed equally to this work

Abstract:

Aerial insects are exceptionally agile and precise owing to their small size and fast neuromotor control. They perform impressive acrobatic maneuvers when they evade predators, recover from wind gust, or land on moving objects. Flapping-wing propulsion is advantageous for achieving flight agility because it can generate large changes of instantaneous forces and torques. During flapping-wing flight, the wings, hinges, and tendons of pterygote insects endure large deformation and high stress hundreds of times each second, highlighting the outstanding flexibility and fatigue resistance of biological structures and materials. In comparison, engineered materials and microscale structures in sub-gram micro-aerial-vehicles (MAVs) exhibit substantially shorter lifespan. Consequently, most sub-gram MAVs are limited to hovering for less than 10 seconds or following simple trajectories at slow speeds. Here, we developed a 750-milligram flapping-wing MAV that demonstrated outstanding lifespan, speed, accuracy, and agility. Owing to transmission and hinge designs that reduce off-axis torsional stress and deformation, the robot achieved a 1000-second hovering flight – two orders-of-magnitude longer than existing sub-gram MAVs. This robot also performed some of the most complex flight trajectories with under 1 centimeter root-mean-square (RMS) error and over 30 centimeter-per-second average speed. With a lift-to-weight ratio of 2.2 and a maximum ascending speed of 100 centimeter-per-second, this robot demonstrated double body flips at a rotational rate exceeding that of the fastest aerial insects and larger MAVs. These results highlight insect-like flight endurance, precision, and agility in an at-scale MAV, opening opportunities for future research on sensing and power autonomy.

One-Sentence Summary: A 750 mg flapping-wing robot demonstrates long endurance flight, precise trajectory tracking, and acrobatic body flips based on offboard power and control.

Main Text:

INTRODUCTION

Insect flight is characterized by fast body dynamics, complex flapping-wing kinematics, and unsteady aerodynamics. Fast neuro reflex and motor control enable aerial insects to quickly evade predators (*1*) and recover attitude stability (*2*). When aerial insects execute banked turns (*3*), body saccades (*4*), or inverted landing (*5*), they experience large rotational speed (>2000 $°s^{-1}$) far exceeding that of birds and micro-aerial-vehicles (MAVs). Aerial insects are also precise flyers when they hover around a flower's anther amid gentle breeze. This exceptional agility and precision are enabled by flapping-wing propulsion that can generate large instantaneous forces and torques. During flight, the insect wing hinge converts the power muscle oscillation into the back-and-forth wing motion ranging from tens to hundreds of times per second. This biomechanical structure is sophisticated and durable. It exerts precise control of wing kinematics through the many steering muscles while it endures large tensile and compressive stress induced by aerodynamic loading and muscle actuation. For instance, the Drosophila wing hinge connects to 12 steering muscles (*6*) and it can control the wing beat motion along all three rotational axes with a fine resolution of less than 2°. When a fly encounters large disturbance, evades predators, or suffers wing damage (*7*), the flapping frequency and amplitude are adjusted over large ranges of 50 Hz and 30°, respectively. Under these harsh mechanical conditions, the hinge can operate millions of wing beat cycles — critical to the survival and functioning of aerial insects.

Inspired by tiny natural flyers, researchers have developed numerous biomimetic MAVs (*8-12*) with the goal of achieving insect-like flight capabilities. Mesoscale (10 – 30 g) flapping-wing robots (*8, 9, 13, 14*) have demonstrated stable hovering flight as well as biomimicking maneuvers such as saccade and body flips. However, owing to larger size and weight, these robots have slower body dynamics. Their wing beat frequency and maximum body angular velocity are substantially slower than that of aerial insects. To miniaturize robot size, electromagnetic motors must be replaced by low friction and power dense microscale actuators. Piezoelectric bimorph actuators (*15*) exhibit high bandwidth and force density, and they lead to a class of sub-gram MAVs (*10, 16-18*). These robots have achieved hovering flight (*10*), trajectory tracking (*16*), and biomimetic demonstrations such as perching (*19*) and hybrid aerial-aquatic locomotion (*20*). Recently, power dense dielectric elastomer actuators (DEAs) were developed and applied in sub-gram MAVs (*21*). The soft actuators exhibited muscle-like robustness and resilience, enabling damage resilience (*22*) and collaborative payload transport (*23*). These advances highlight the unique flight capabilities of sub-gram MAVs in comparison to mesoscale aerial robots.

However, the flight performance of aerial insects remains far superior to that of sub-gram MAVs. Aside from relying on offboard power and control, sub-gram MAVs have limited flight endurance, speed, accuracy, and agility. This performance gap is largely contributed by the lack of fabrication methods and engineered materials for building similar biomechanical structures in insects. While the Smart Composite Manufacturing (SCM) (*24*) method can fabricate 3D structures with micron-level resolution, it remains difficult to incorporate compatible materials that exhibit high flexibility and durability. For example, elastomeric protein resilin is a durable, elastic, and low loss material found in insect wing hinge ligament. It can be stretched up to 3 times and shows a fatigue limit of 300 million cycles (*25*). In contrast, biomimetic flexures in MAVs are built with thin film polyimide whose elongation ratio and fatigue limit are merely 0.72 and 300,000 cycles. Under a similar geometry, the transmission and hinge in sub-gram MAVs exhibit substantially shorter lifespan. Owing to this materials challenge, most existing sub-gram MAVs (*26*) are limited to short flights within 10 seconds, and they require frequent tuning and repair. The lack of flight endurance also constrains other flight capabilities. Given a short lifespan, it becomes difficult to accurately estimate the robot's inertial parameters, measure force and torque mappings, and develop well-tuned controllers. Most sub-gram MAVs (*10, 16, 27*) are limited to performing hovering flights or following simple trajectories at a speed lower than 10 cm·s^{-1}. In the rare example of performing a somersault (*28*), prior robots cannot recover attitude stability before rebounding on the floor, which is caused by inaccurate force and torque mappings under a limited number of characterization experiments. These limitations underscore the importance of developing a durable sub-gram MAV, which is critical to improve flight speed, accuracy, and agility.

In this work, we developed a 750 mg four-winged MAV (Fig. 1A-B) with outstanding flight endurance, speed, accuracy, and agility. We identified off-axis loading as the main contributor to flexure fatigue and failure, and then designed airframe, transmission, hinge, and wing (Fig. 1C) to minimize off-axis torsion. The robot demonstrated a 1000-s hovering flight – two orders of magnitude longer than most existing sub-gram MAVs. This long lifespan allows extensive robot characterization and leads to a new flight controller that improves flight precision under dynamic conditions. The robot demonstrates a sequence of trajectory-tracking flights with sub-centimeter accuracy and an average speed of 30 cm·s^{-1}, representing the most accurate and fastest flights performed by a sub-gram MAV. As an example, Fig. 1D shows a composite image where the robot follows the letters "MIT", with a root-mean-square (RMS) position error of 0.73 cm. Furthermore, the robot design enabled acrobatic maneuvers through reducing moment of inertia and increasing body torque generation. With a lift-to-weight ratio of 2.2 and a maximum ascending speed of 100 cm·s^{-1}, the robot achieved a double flip within 0.17 second. During this maneuver, the maximum body roll rate exceeds 7200 °s^{-1}, which is 40% faster than fruit flies (*5*) and quadruples that of the fastest aerial robot (*29*). These flights showcase insect-level performance in a sub-gram MAV, and they also open opportunities for future research on sensing and power autonomous microsystems.

RESULTS

Design of a long endurance and agile flapping-wing robot

Compared to aerial insects, prior sub-gram MAVs have limited flight time and agility. We designed a four-winged aerial robot (Fig. 1A) that can demonstrate long flight endurance and acrobatic maneuvers. The 750-mg robot has four identical modules with a compact dimension of 4 cm × 4 cm × 0.9 cm (Fig. 1B). Each module consists of an airframe, a DEA, a set of transmissions, and a wing with its long hinge (Fig. 1C).

The module is designed to maintain high structural consistency under the large stress and strain induced by the flapping-wing motion. The cylindrical DEA has a diameter and length of 5.8 mm and 5 mm, respectively. Compared to rigid actuators, DEAs have lower modulus and they are susceptible to off-axis deformation (*21*). The carbon fiber airframe (Fig. 1C and fig. S1A) consists of six I-beams to minimize structure oscillations during DEA actuation. Three sets of linear four-bar transmission connect the DEA to the airframe. In addition to converting the DEA's linear elongation to the wing rotational motion (*21*), the transmissions reduce the DEA off-axis deformation by constraining it along the longitudinal axis. The wing has a long hinge along its leading edge (Fig. 1C) to endure the stress and strain of flapping. Compared to the shorter wing hinges in prior works (*21, 30*), this new design reduces the hinge stress by over 1000 times, leading to a substantial increase of hinge lifespan.

This modular design also enables precise and agile flight maneuvers by reducing robot moment of inertia and increasing flight torque generation. Compared to rotary designs where the motor and the propeller are placed along the same axis, flapping-wing designs offset the wing from the actuator. In our robot, the distance from the robot center of mass (COM) to each module's COM and center of pressure (COP) are 8.7 mm and 22.5 mm, respectively (Fig. 1C). The robot has small moments of inertia owing to the small distance between the robot COM and each module's COM, yet it can generate large body torques due to the large robot COM to COP distance. Consequently, this design allows the robot to generate large angular acceleration under small changes of lift forces, which enable aggressive control and fast maneuvers. The main robot design parameters include the transmission ratio, wing size, and hinge stiffness. A detailed description of parameter selection is given in Supplementary Discussion S1 and fig. S2.

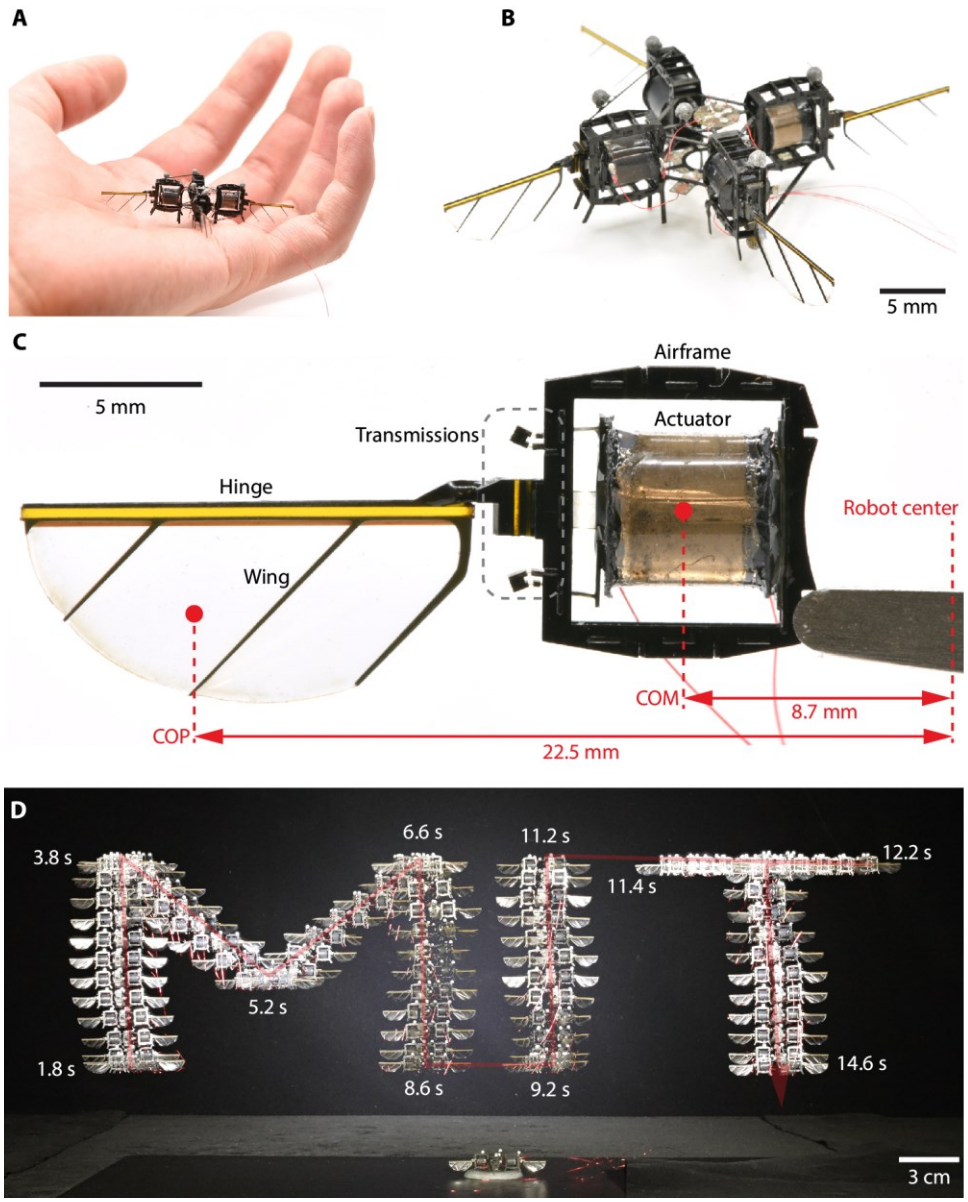

Fig. 1. A long endurance, precise, and agile insect-scale flapping-wing robot. (**A**) An image of the robot resting on a human palm. (**B**) This 4 cm × 4 cm × 0.9 cm robot consists of four identical modules. (**C**) Each robot module has a soft actuator, an airframe, a set of transmissions, and a wing with a long hinge. (**D**) A composite image of a trajectory tracking flight in which the robot traces the letters "MIT".

Static characterization of robot performance

We conducted a series of statically constrained experiments (Fig. 2A-C, fig. S2A-C) to evaluate robot performance. Fig. 2A and movie S1 part 1 show a static flapping-wing experiment where the DEA operates at 1925 V and 330 Hz. Like prior designs (*21*), the flapping-wing motion has two degrees of freedom: the wing stroke and pitch motion. The DEA oscillation directly drives the wing stroke motion while the wing pitch motion is passive. The instantaneous wing stroke and pitch angles are shown in Fig. 2D and their peak-to-peak amplitudes are 41° and 118°, respectively. Compared to that of prior designs, the stroke amplitude becomes substantially smaller to reduce flexural strain in the four-bar transmission. This reduction of stroke amplitude was compensated by two times increase of the wing area, which generates sufficient lift forces for enabling flight. To measure the net lift force, we mounted the robot on a beam that was balanced around a pivot. We operated the robot at the same condition of 1925 V and 330 Hz and filmed its liftoff process (Fig. 2B and movie S1 part 2). The robot ascends 5.2 cm in 0.6 s while it carries a 360 mg payload inclusive of its weight. Through tracking the robot liftoff angle and fitting to a dynamical model (*28*), we measured the net lift force to be 4.0 mN – equivalent to a lift-to-weight ratio of 2.2.

To characterize robot performance across different operating conditions, we varied the driving voltage and frequency in static flapping and liftoff experiments. Fig. 2E shows flapping experiments where voltage and frequency were set independently in the range of 1300 V to 1925 V and 100 Hz to 500 Hz. The wing stroke amplitude reaches a maximum near 300 Hz, which implies the net lift force also maximizes around similar frequency. Next, we repeated liftoff tests (Fig. 2B and movie S2 part 2) under different driving conditions. Fig. 2F shows the measured lift force as functions of driving voltage and frequency and it reaches maximum at the 330 Hz condition. Based on this result, we fixed the operating frequency to 330 Hz for all flight experiments. The red curve in Fig. 2F represents the voltage-to-lift force mapping applied in the flight controller. Similar to prior works (*28, 30*), we modeled the DEA as a series resistor-capacitor (*RC*) element and found the equivalent *R* and *C* to be 78 kΩ and 1.48 nF, respectively. The

330 Hz operating condition is close to the mechanical resonance frequency determined by the wing-transmission-actuator system, while the electrical resonance frequency is over 1 kHz as predicted by the *RC* time constant. Using a custom circuit, we measured the robot power consumption during liftoff flight and obtained a lift-to-power ratio of 9.4 mN W^{-1}. The robot efficiency is similar to our prior works (*28, 30*) but approximately 5 times worse than piezoelectric flyers (*10*).

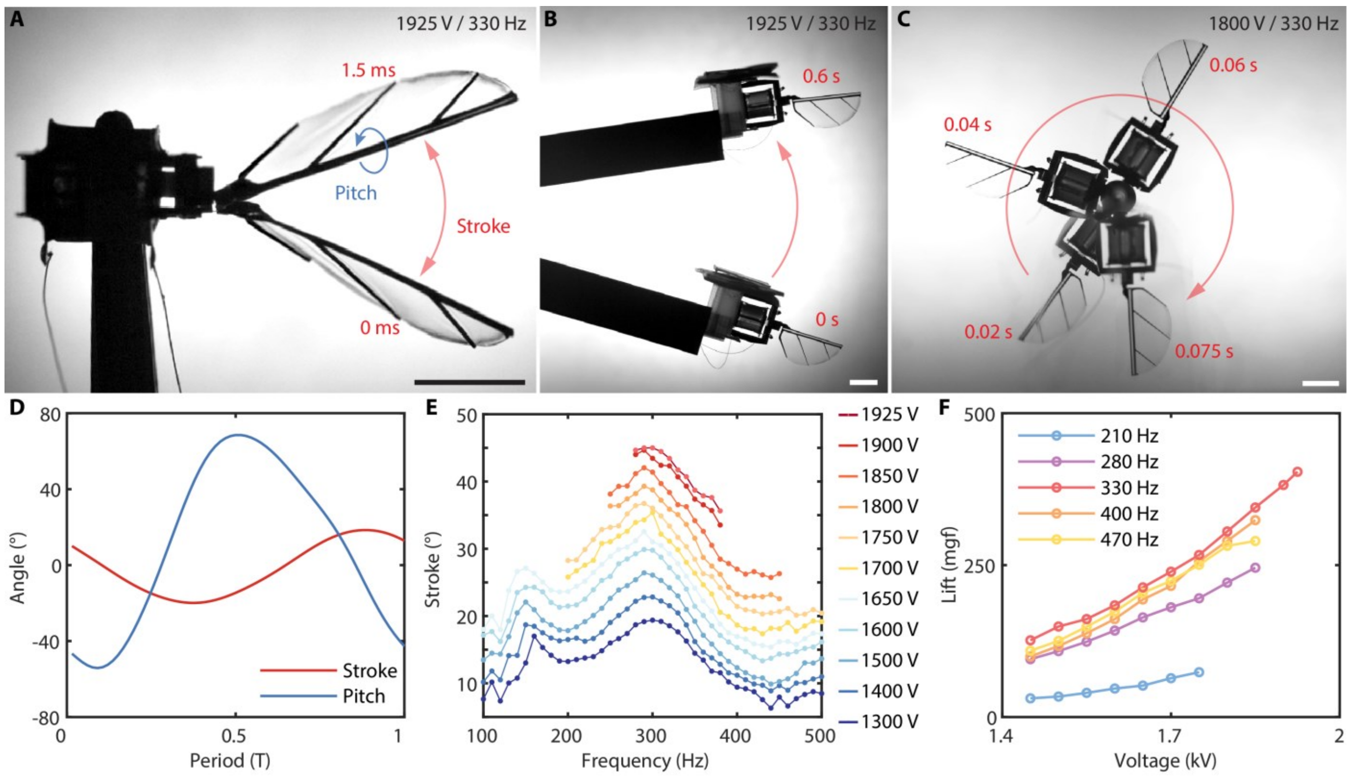

Fig. 2. Static characterization of robot performance. (**A**) A composite image of the robot flapping-wing motion when it operates at 1925 V and 330 Hz. (**B**) A composite image of robot liftoff when it carries 180 mg payload. The robot achieves a maximum lift-to-weight ratio of 2.2. (**C**) A composite image of robot rotation experiment. (**D**) Measured instantaneous wing stroke and pitch motion that correspond to (A). (**E**) Robot stroke amplitude as functions of operating voltage and frequency in flapping experiments. (**F**) Robot lift force as functions of driving voltage and frequency in liftoff experiments. Each dot in (E-F) corresponds to a separate experiment where the driving frequency and voltage are set independently. The scale bars in (A-C) represent 5 mm.

Next, we characterized robot torque generation by mounting it around a fixed post and measuring its rotational speed (Fig. 2C). When the robot was driven at 1800 V and 330 Hz, it revolved around the post 4 times in 0.205 seconds (Fig. 2C and movie S1 part 3). By tracking the instantaneous rotation angle (fig.

S2I), we measured an average angular acceleration of 46200 $°s^{-2}$. The maximum angular speed reaches 9700 $°s^{-1}$, which implies the robot can generate large body torque and perform aggressive maneuvers.

In addition to quantifying robot force and torque production, we demonstrated substantial improvement of robot actuation consistency and lifespan. The prior wing hinge design (Fig. 3A) mimics the relative dimension of an insect wing hinge (*6*), which is less than 20% of the wingspan. While resilin protein in the insect hinge can endure large cyclic loading and deformation, the polyimide flexure in the robot hinge has a far shorter fatigue limit. We conducted numerical simulation where a static load was applied at the wing's COP. The static loading force is set to 5 mN, equivalent to the estimated drag force during hovering flight (*31*). The insets in Fig. 3A show that stress is concentrated near the hinge's lower left and upper right corners, which suggests cracks may initiate along these high-stress regions.

To verify this simulation result, we conducted static flapping-wing experiments with the wing hinge pair in Fig. 3A. We drove the wing at the robot liftoff condition until we observed sudden hinge failure (Fig. 3B-C and movie S2 part 1). In this experiment, the flapping-wing motion became anomalous after approximately 200 seconds, and then a crack quickly developed and propagated through the entire hinge. Fig. 3B shows an image of the torn hinge that failed within 4 wingbeats (Fig. 3C). This sudden hinge failure would immediately lead to a loss of lift force, further destabilizing flight (movie S2 part 2). This hinge fatigue problem exacerbates as the wing size increases. Under the same wing hinge, we found the hinge lifespan decreased by 10 times when the wing area was scaled up by 2 times (fig. S1F).

To address this problem, we redesigned the wing hinge to reduce flexural stress. In the new design, the polyimide flexure extends through the entire wing (Fig. 3D). In comparison, the distance from the wing COP to the hinge center is reduced from 5.5 mm (Fig. 3A) to 0.7 mm (Fig. 3D). Numerical simulation shows the maximum hinge stress reduces by over 1000 times. Following this simulation result, we conducted static flapping and flight experiments to measure the new hinge lifespan. After enduring over 1000 seconds of static flapping and 1500 seconds of flight experiments, the new wing and hinge did not exhibit any degradation or failure. This is an important result because the robot would no longer suffer sudden wing loss during flight.

Our robot design also mitigated performance degradation due to off-axis actuator bending. The DEAs are muscle-like soft actuators that elongate along the axial direction. However, large axial load due to the aerodynamic forces may lead to dynamic buckling (*21*) along the off-axis direction. In the original design, the linear four-bar transmission is compliant in the off-axis direction (Fig. 3E). When the robot operates near peak performance conditions, the DEA deforms laterally (Fig. 3E and movie S3), which reduces the wing stroke amplitude and the associated lift force. This off-axis DEA bending may also lead to electrical shorting and degrade DEA performance.

To mitigate this problem, we added two guide transmissions that constrain DEA off-axis bending (Fig. 3F). Fig. 3F and movie S3 show the new robot was operated at the same condition of 1850 V and 330 Hz. Compared to the old design (red curve in Fig. 3G), the new design shows a 78% decrease in off-axis displacement and 87% increase in axial elongation. This translates to over 80% increase in wing stroke amplitude, suggesting a large increase in lift force production. This addition of guide transmissions increases robot lift force at peak operating conditions, reduces transmission deformation, and improves robot endurance. In addition, the robot actuator, transmission, and hinges consist of compliant materials that exhibit collision resilience. While the robot operates at 1800 V and 330 Hz, we hit the robot wing with a stick (Fig. 3H and movie S1 part 4), which reduced the wing stroke motion. After the stick was removed, the robot flapping-wing motion recovered to the nominal amplitude within four wingbeats (Fig. 3H-I), indicating the robot is robust against collisions.

With this new robot design, we performed constrained liftoff experiments (Fig. 2B) to quantify DEA degradation. The robot was mounted on the liftoff stand and it was driven at 330 Hz and the minimum liftoff voltage for 10 seconds. If the robot could lift off, then we repeated the experiment at the same operating condition. If the robot could not lift off, then we increased the driving voltage by 10 V. We repeated the experiments until the robot completed 1000 seconds of cumulative liftoff flight. Fig. 3J showed the commanded voltage (blue) and the measured current (red). Over the 1000-s operation, the minimum liftoff voltage increased by 4.8% and the current reduced by 4%. This data shows the robot's potential to operate for an extended duration far exceeding tens of seconds.

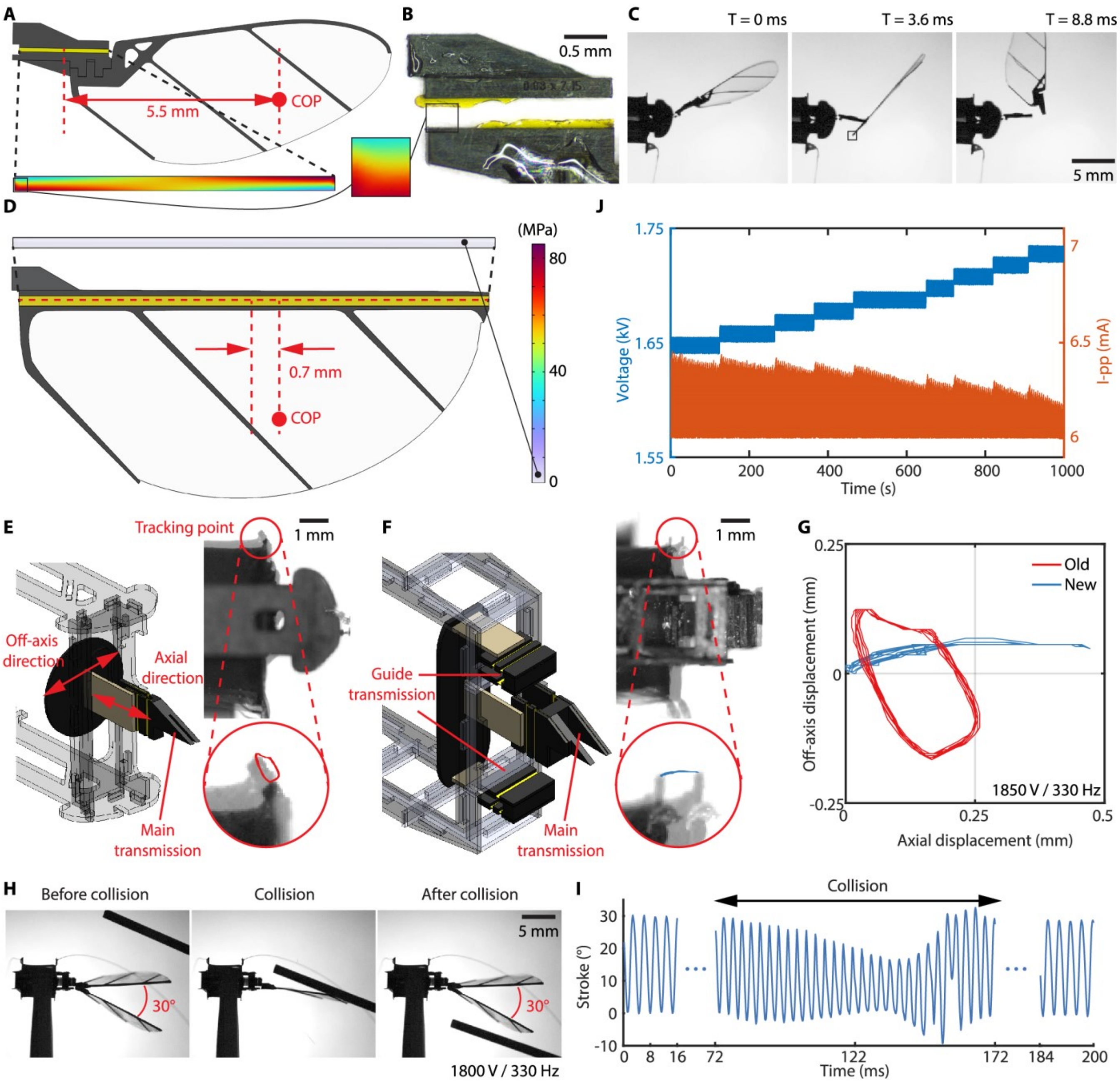

Fig. 3. Experimental characterization of wing hinge and transmission performance. (**A**) An illustration of the prior wing and hinge design. The inset shows a COMSOL simulation of hinge stress when the robot operates at the hovering condition. High stress concentrates near the hinge root (left) and tip (right). (**B**) An image of the torn hinge. (**C**) An image sequence that shows sudden wing hinge failure. (**D**) An illustration of the new wing and hinge design. The inset shows a COMSOL simulation of hinge stress under the same operating condition as in (A). The stress concentration plots in (A) and (D) share the color scale, which shows the maximum stress in (D) reduces by over 1000 times. (**E**) A prior design

of the linear four bar transmission. The overlaid image shows large actuation hysteresis. (**F**) A new transmission design that constrains off-axis motion. The overlaid image shows DEA actuation is mostly axial. (**G**) Comparison of DEA deformation under different transmission designs in (E) and (F). (**H**) The robot wing was hit by a stick while it operated at 330 Hz with 30° stroke amplitude. The flapping-wing motion recovered to nominal amplitude after the stick was removed. (**I**) The measured wing stroke motion before, during, and after collisions. (**J**) Commanded voltage amplitude and measured current during a 1000-s static liftoff experiment.

Long endurance hovering flight

We conducted a sequence of hovering flights to evaluate robot endurance. In our flight experiments, the robot is tethered to offboard power sources (Trek 2220) and relies on an external motion capture system (Vicon Vantage V5). We designed a feedback flight controller that receives tracking data at 400 Hz and commands the robot at 2 kHz. Compared to prior work (*21*), this controller introduces three features for reducing positional error during dynamic maneuvers. The controller implementation details are described in Supplementary Discussion S2.

To assess robot consistency and lifespan, we gradually increased the flight time from 10 s, 60 s, 100 s, 400 s to 1000 s. The shorter flights are described in Supplementary Discussion S3 and fig. S3. Fig. 4A shows a composite image sequence of the 1000-s flight (movie S4) where the robot hovered 7 cm above ground. The RMS error of lateral position (Fig. 4B) and altitude (Fig. 4C) are 2.35 cm and 0.14 cm, respectively. Compared to most prior results (*21, 28, 30*), the flight time increases by 100 times while the robot maintains similar flight accuracy. During this flight, the robot slowly drifts along the positive x and negative y directions (Fig. 4B), which is contributed by gradual DEA heating and degradation. Fig. 4D shows the driving voltage amplitude of the four actuators. Over this 1000-s flight, the commanded voltage of the first DEA (dark green curve in Fig. 4D) increases from 1720 V to 1850 V, representing a 7.56% deviation from the calibrated controller values. This performance degradation was likely contributed by self-clearing during flight and the DEA did not recover to nominal performance after cooling down to room temperature. The lateral position error could be further reduced under an adaptive flight controller that accounts for changing performance.

Overall, this 1000-s flight represents orders-of-magnitude improvement in hovering time among sub-gram MAVs. Before requiring actuator replacements, the robot performed consecutive long flights where the total hovering time exceeded 1550 seconds. Unlike prior designs (movie S2 part 2), this robot never experienced sudden hinge or actuator failure that could destabilize the flight. This high consistency and long lifespan enabled follow-up experiments on complex trajectory tracking and aggressive acrobatics.

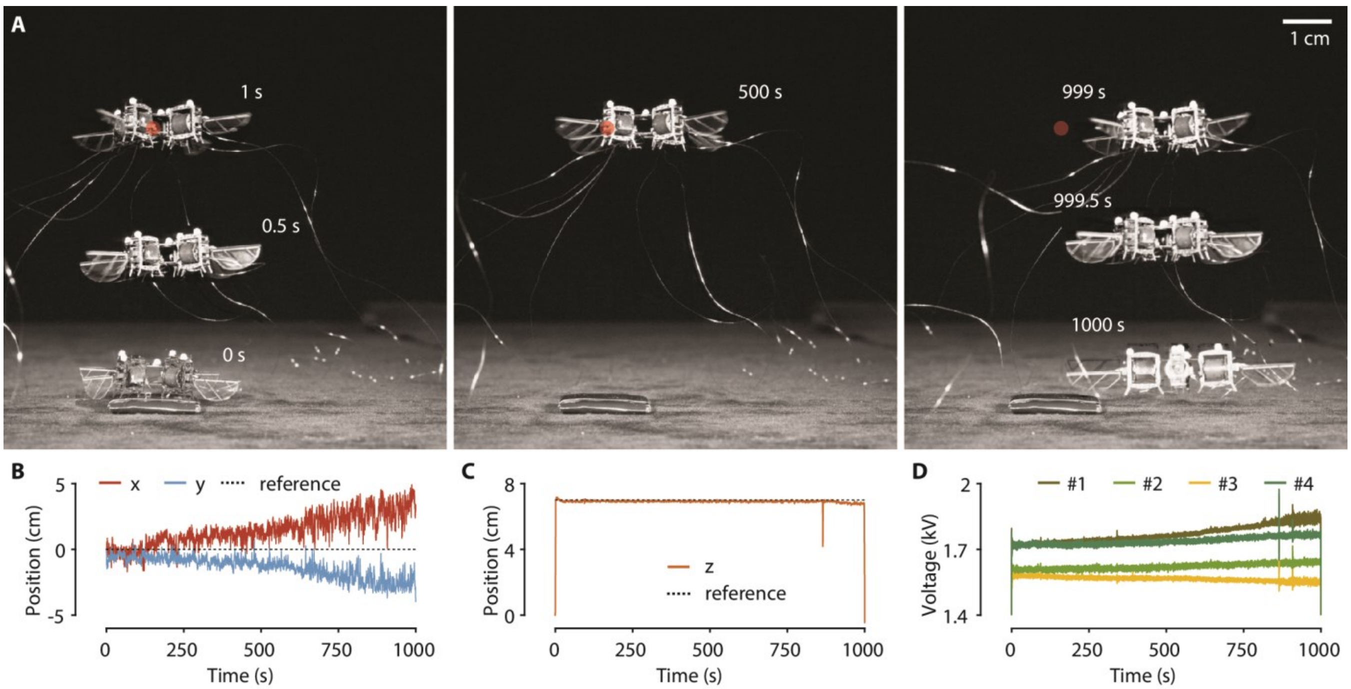

Fig. 4. A 1000-s, long endurance hovering flight. (**A**) A composite image sequence that shows the 1000-s hovering flight. (**B-C**) Tracked robot lateral position (B) and altitude (C) during the flight. (**D**) Commanded voltage amplitudes sent to the four independent actuators.

Fast and precise trajectory tracking flights

In addition to achieving long endurance flights, we performed a sequence of trajectory tracking demonstrations that highlight robot precision and speed. First, our robot tracked a 20 cm × 10 cm "∞" sign similar to that of a recent work (*16*). While performing this flight (Fig. 5A and movie S5), the robot closely followed the desired x and z trajectories (Fig. 5B-C) with lateral and altitude errors of 0.97 and 0.29 cm, respectively. The average flight speed reached 31.4 $cm \cdot s^{-1}$ (Fig. 5D) while the robot tracked the infinity sign. Compared to a recent work (*16*), our robot tracks the same trajectory with 3.1 times faster speed yet the position and altitude error are reduced by 61.8% and 42%, respectively. This benchmark flight shows the highest flight precision and speed among sub-gram aerial robots. To demonstrate robot consistency, we repeated the same flight five times (fig. S4).

Next, our robot tracked two nested circles that are 10 cm above the xy-plane (Fig. 5E and movie S6). The outer circle has a dimension of 12 cm × 12 cm, and the robot followed it with a speed of 36 $cm \cdot s^{-1}$ and a positional error of 0.91 cm for the entire flight. Compared to a prior work that tracked a similar trajectory (*32*), our robot demonstrates 5 times reduction of RMS position error (Fig. 5F-G) at 8 times higher flight speed (Fig. 5H). This flight was repeated five times (fig. S5) to highlight robot and controller consistency.

In addition to tracking simple trajectories (Fig. 5A-H), our robot can follow complex paths that are difficult for other sub-gram robots. We designed a 20 cm × 20 cm × 10 cm 3D trajectory where an infinity sign gradually rotated along the z-axis (Fig. 5I and movie S7). The robot tracked the rotating pattern 15 times during a 34-s flight. Figure 5J-K show the measured x, y, and z positions closely follow the desired path. The robot maintained a mean speed of 30 $cm \cdot s^{-1}$ (lower panel in Fig. 5K) while it tracked this 9.7 m long trajectory — the longest flight path flown by a sub-gram MAV. The RMS lateral position and altitude errors of this flight are 1.05 cm and 0.34 cm, respectively. This flight was repeated five times (fig. S6).

Our robot achieved smaller position and altitude errors when it flew at a slower speed. To demonstrate high flight precision, we commanded the robot to trace the letters "MIT" (Fig. 1E and movie S8) at a slower speed of 7.48 $cm \cdot s^{-1}$. This trajectory has a dimension of 46 cm × 12 cm, and it is challenging due to frequent stopping and changing of flight directions. Fig. S7 shows the six flights our robot has performed, with a mean RMS lateral position and altitude error of 0.80 cm and 0.20 cm, respectively. Compared to the 3D trajectory in Fig. 5I, the position and altitude error reduce by 24% and 41%, respectively. The lateral position and altitude errors of all four trajectory following flights are compared in Fig. 5L-M, which show the flight precision improves when flight speed reduces. The 3D infinity and letter following flights represent some of the longest and most complex paths flown by sub-gram MAVs.

These demonstrations are enabled by the robot's high consistency and its ability to generate large body torques. The trajectory design is described in Supplementary Discussion S4.

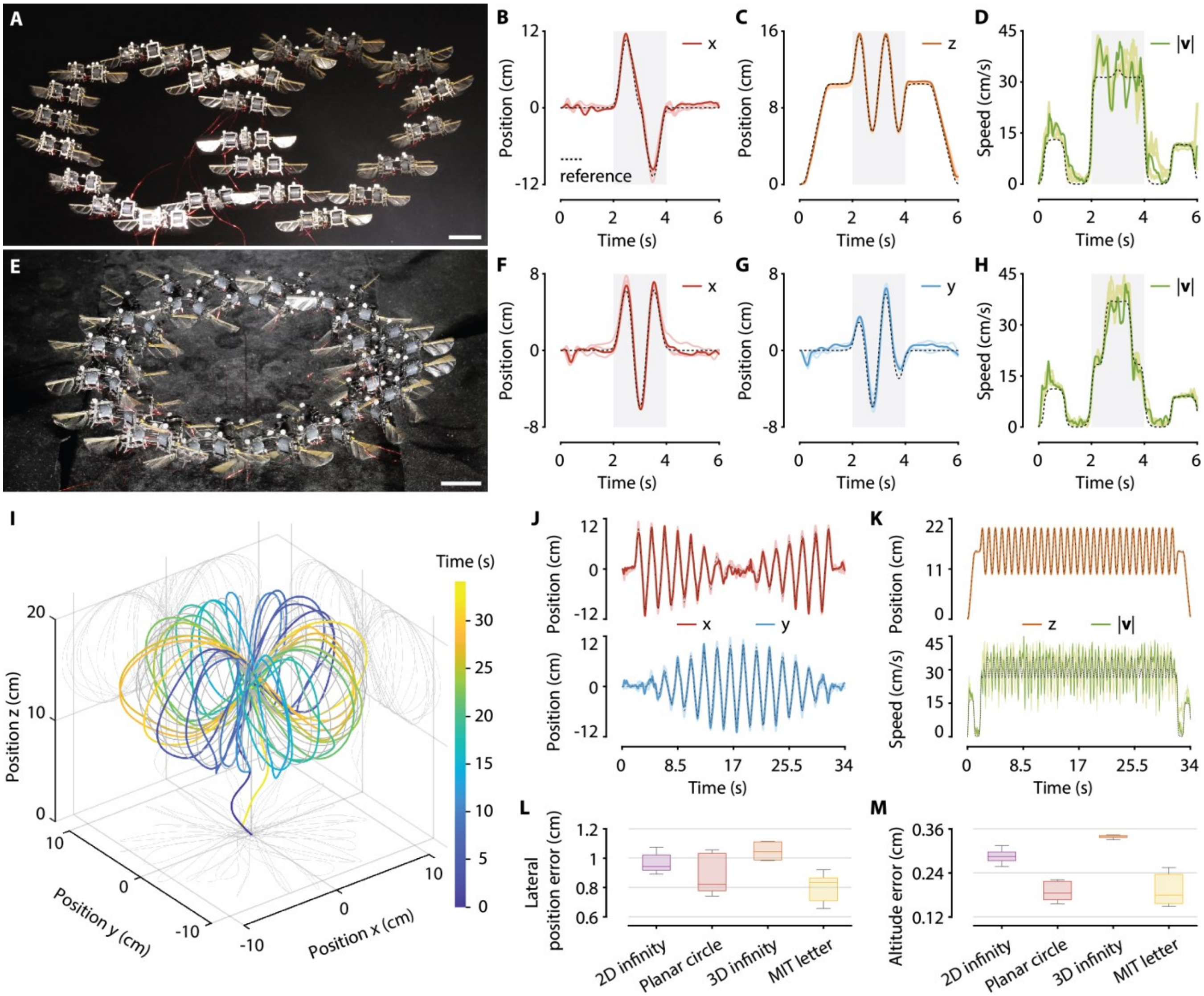

Fig. 5. Trajectory following demonstrations. (**A**) A composite image of the robot following an infinity sign. (**B-D**) Robot x (B), z (C) positions, and flight speed (D) that correspond to the flight in (**A**). (**E**) A composite image of the robot tracking a planar circle. (**F-H**) Robot x (F), y (G) positions, and flight speed (H) that correspond to the flight in (E). (**I**) The tracked trajectory when the robot follows a rotating infinity pattern. (**J-K**) Robot x, y, and z positions, and the flight speed that correspond to the flight in (I). The trajectory following flights in (A), (E) and (I) were repeated five times. The darker colored curves in (B-D), (F-H), and (J-K) correspond to the flight in (A), (E), and (I), respectively. The lightered colored curves represent the repeating flights. (**L-M**) RMS lateral (L) and altitude (M) error of the four trajectories. The standard deviation and mean values are computed based on the five repetitions. The scale bars in (A) and (E) represent 1 cm.

Demonstrations of acrobatic flight maneuvers

In addition to performing fast and precise flights, our robot can demonstrate insect-like acrobatic maneuvers (movie S9-10). Fig. 6A-C show a composite image sequence of a somersault demonstration. The robot takes off and hovers around a setpoint for 1 s (Fig. 6A). Next, it accelerates upward until the ascending speed exceeds 80 $cm \cdot s^{-1}$. Then it performs the somersault within 0.11 s (Fig. 6B) and recovers attitude stability (Fig. 6C). Finally, the robot returns to the hovering setpoint and lands (Fig. 6C). Fig. 6D-F show the tracked robot position, altitude, attitude, flight velocity, and angular velocity. This flight is repeated five times (fig. S9) to demonstrate robot consistency. The controller design is described in Supplementary Discussion S5 and fig. S8.

This flight shows a complete body flip performed by a sub-gram MAV. In a prior work (*28*), another sub-gram MAV demonstrated a body flip but it could not recover altitude before hitting the ground. In comparison, this robot can recover attitude stability without dropping height (upper panel in Fig. 6E). The robot completes the somersault within 0.11 s – the fastest among all existing aerial robots. During this maneuver, the maximum robot angular velocity exceeds 4800 $°s^{-1}$.

Our robot can further perform double body flips – a challenging maneuver that has never been achieved by flapping-wing robots across scales. Fig. 6G-I show a composite image sequence of this flight. Similar to the single body flip, the robot takes off, hovers, ascends, flips, recovers stability, and finally lands. The measured robot position, velocity, attitude, and angular velocity are shown in Fig. 6J-L. In this flight, the robot completes two body flips with 0.17 s. When the robot accelerates upward, its maximum ascending speed exceeds 100 $cm \cdot s^{-1}$. During the flipping process, the robot's maximum angular velocity reaches 7200 $°s^{-1}$ (lower panel in Fig. 6L). After the robot recovers its attitude stability, it only loses 6.22 cm of height (upper panel in Fig. 6K) compared to the start of the flip. These flight performances far exceed existing sub-gram MAVs and they are comparable to that of aerial insects (*5*). The fast robot speed and turning rate also make it among the most agile soft-driven robots. This highly acrobatic flight is repeated five times (fig. S10) to demonstrate robot consistency under aggressive operating conditions.

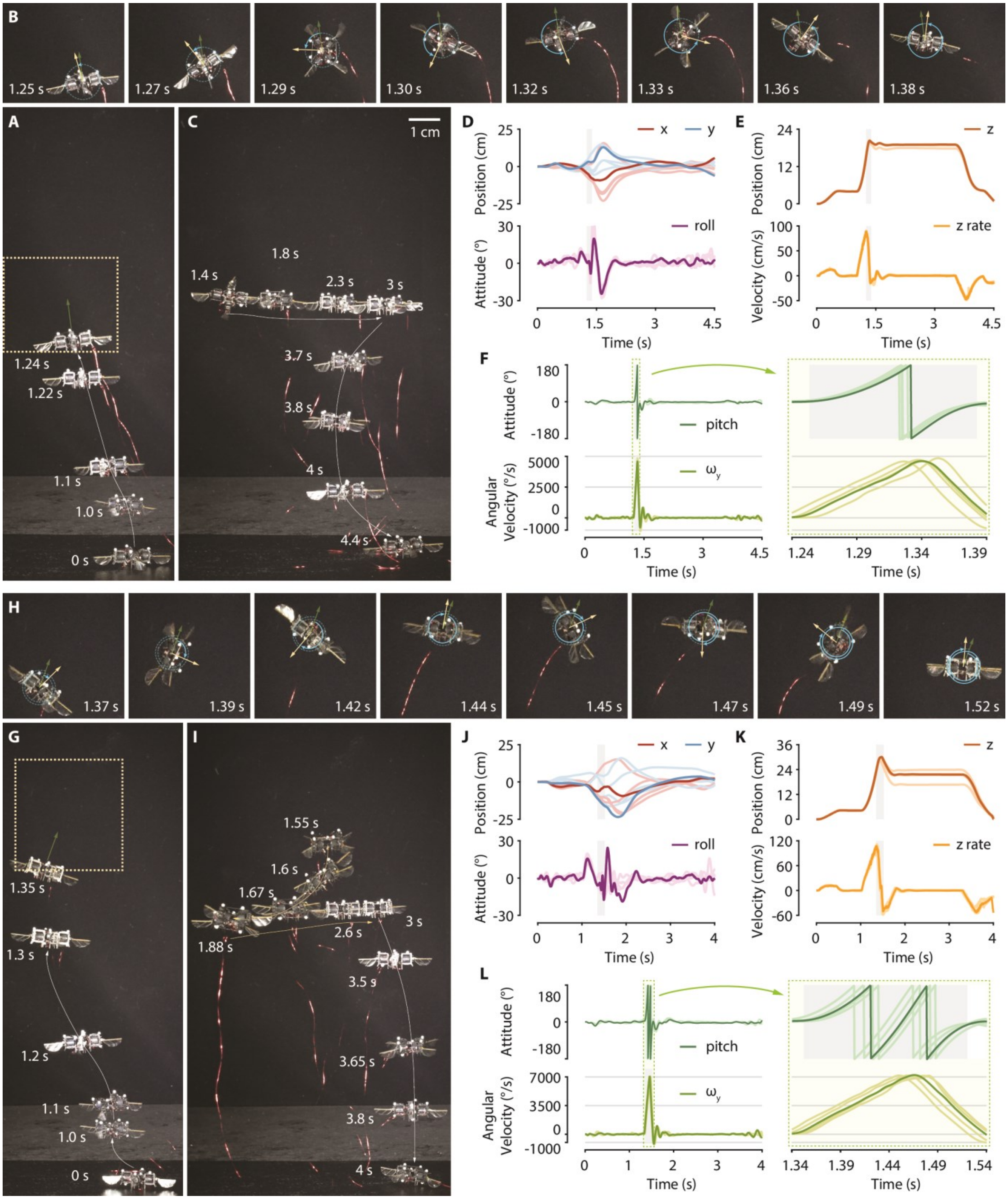

Fig. 6. Acrobatic flight demonstrations. (**A-C**) The robot performs a single body flip including ascent (A), body flip (B), recovery (C), and landing. (**D**) Tracked robot lateral position and roll angle. (**E**) Tracked robot altitude and ascending speed. (**F**) Robot pitch angle and angular speed. (D-F) corresponds to the flight in (A-C). (**G-I**) The robot performs double body flips including ascent (G), consecutive body flips (H), recovery, and landing (I). (**J-L**) Tracked robot lateral position and roll angle (J), altitude and ascending speed (K), and pitch angle and angular velocity (L). (J-L) corresponds to the flight in (G-I). The single and double flips were repeated five times. In (D-F) and (J-L), the darker colored curves

represent the flight data in (A-C) and (G-I). The lighter colored curves are the repeating flights. The scale bar in (C) applies to (A-C) and (G-I). In (A) and (G), the rectangular regions represent the same cropped regions in (B) and (H) where the robot performs the flips. In (B) and (H), the green and yellow arrows indicate the start and instantaneous robot orientations, respectively.

DISCUSSION

In this work, we developed a soft-actuated MAV that exhibits long endurance, high flight precision, and insect-like agility. These flight capabilities were enabled by new mechanism, configuration, and controller designs. Stress-relieving transmissions and hinges substantially improved the hardware consistency; the four-wing configuration enhanced lift force generation through avoiding adverse wing-wing interactions that relate to the inward facing wing pairs in prior eight-wing designs *(21)*. These hardware designs resulted in remarkable improvements of flight endurance and maximum ascending speed. In the past, sub-gram MAVs were limited to flying for less than 20 s at low speeds (blue dots in Fig. 7A). Our robot showed a 1000-s hovering flight – almost two-orders-of-magnitude longer than most sub-gram MAVs. In addition, its ascending speed exceeds 100 $cm \cdot s^{-1}$ – twice that of similar sized rigid-driven MAVs. In addition to hardware advances, we designed a new controller for improving flight precision, which could be quantified by measuring the position error of hovering or trajectory following flights. The position error usually increases in faster and longer flights due to unaccounted aerodynamic effects and hardware drifting. In the past, sub-gram MAVs were limited to slowly (<15 $cm \cdot s^{-1}$) following short (<20 s) trajectories and their position error ranged from 1.2 to 4.5 cm (blue dots in Fig. 7B). Our robot demonstrated much faster (>30 $cm \cdot s^{-1}$) trajectory tracking flights with smaller position errors (red dots in Fig. 7B). The error in most flights was smaller than 1.4 cm (Fig. 7B), and it grew to 2.3 cm in the 1000-s hover due to slow DEA degradation. Our flight trajectories were also more challenging because they had frequent turns and longer pathlengths (Fig. 5). Overall, our new robot and controller design achieved substantial improvements in flight endurance, speed, and precision (Fig. 7A-B).

Furthermore, high hardware consistency and precise flight control enabled insect-like agility. Our robot demonstrated double body flips – a challenging acrobatic maneuver that has never been shown in existing flapping-wing robots across scales. This performance is competitive against rotary MAVs and natural flyers (Fig. 7C). Inertial scaling predicts the robot's rotational speed is inversely proportional to the wing or rotor size, suggesting smaller robots can perform somersaults at a faster rate. This trend is supported by Fig. 7C, which shows our robot achieves the fastest rotation compared to existing drones (blue). Remarkably, our robot is also faster than the Blue bottle fly – the fastest flipping aerial insect (*5*).

These flight demonstrations have far-reaching implications for the microrobotics and the soft robotics communities. Achieving insect-like endurance, precision, and agility opens opportunities for emulating complex insect functions. It will inspire the sub-gram MAV community to move from hovering or simple trajectory following demonstrations to accomplishing complex and extended tasks such as pollination and coordinated swarm flights. From the perspective of the soft robotics community, this work demonstrates controllability and agility comparable to that of rigid-driven systems. In the past, robustness and safety were salient features of soft actuators and mechanisms (*33*), but soft robotic systems fell behind in bandwidth and agility. Compared to existing soft robots, this tiny robot achieves some of the fastest speed and turning rate without requiring normalization by its body length. It demonstrates soft-driven robots can simultaneously embody robustness and agility. During the body flip maneuver, the DEAs respond to aggressive driving signals within milliseconds while they endure high stress and strain. These muscle-like properties outperform rigid actuators such as piezoelectric ceramics and microscale motors. This work will inspire future development of high-power soft actuators (*34*) and their applications in agile animal-like systems.

The substantial improvements in endurance, precision, and agility (Fig. 7A-C) were enabled by new robot designs that carefully considered the similarities and differences between biological and engineered systems. Our goal is to achieve insect-like flight performance in insect-scale robots, and it requires both biomimicking designs and engineered solutions. At this scale, rotary propulsion becomes infeasible due to a lack of efficient microscale motors. We chose the flapping-wing design and developed robust and muscle-like DEAs. These soft actuators have high resonance frequencies of 300 – 500 Hz, which implies the robot can generate large instantaneous changes of forces and torques. In addition, flapping-wing

MAVs are tolerant to collisions due to the reciprocal wing motion and the robot's low inertia. The use of artificial muscles and flapping-wing propulsion represents suitable biomimicking designs for achieving biomimetic functions.

However, under material and actuation constraints, it is also critical to adopt engineered designs that deviate from that in biological systems. For instance, insect hinges consist of resilin protein that exhibit high fatigue limit under large cyclic loading and strain. In contrast, polyimide has 4 times lower elongation ratio and 1000 times lower fatigue limit. Under a similar geometry, the robot hinge and transmission would experience failure (Fig. 3B) within 200 s. Our new design reduced the hinge flexural stress by 1000 times through elongating the hinge width. It also reduced the transmission strain through decreasing the flapping-wing amplitude and maintained similar lift force through proportionally increasing the wing area. This wing hinge and transmission design principle can also benefit other sub-gram MAV platforms. Piezoelectric driven MAVs *(10, 16, 19)* have a limited lifetime due to actuator cracking, which is caused by resonance mismatch when the flexures gradually soften. Elongated wing hinge and new guide transmission designs can mitigate flexural degradation and contribute to longer endurance. Another design choice that deviates from biology is the use of four independently controlled wings. Insects have delicate muscle groups that exert fine control of the flapping-wing motion, but it is difficult to develop differently sized actuators and delicate transmissions for achieving 3 degrees-of-freedom (DoF) control of wing kinematics. We used four sets of actuators and wings to generate roll and pitch torques, which allowed the robot to achieve insect-like agile maneuvers and precision. This work demonstrates challenging bio-inspired locomotive capabilities by combining biomimicking and engineered designs.

Despite showing a large improvement of flight endurance, our robot lifetime remains 2-3 orders of magnitude shorter than that of mesoscale aerial robots – limiting potential applications. The robot has three failure modes: transmission softening, wing hinge tearing, and DEA degradation. In our prior works, wing hinge and transmission failure were the major limiting factor (80,000 flapping-wing cycles) while the DEAs only experienced 2% performance reduction after 2 million cycles of operation (30). In this work, we redesigned the transmission and wing hinge to reduce the flexural stress, which substantially improved the hinge and transmission endurance. We have not observed hinge or transmission failure in this work. However, the reduction of transmission ratio led to higher actuation strain and required higher driving voltage. Compared to our prior work (30), the robot hovering voltage increased from 1500 V to 1720 V. This high operating voltage caused 7.56% DEA degradation during the 330,000 cycles of operation, implying the robot lifetime was limited by the actuator. There are two directions for further improving the robot lifetime. In the short term, the robot design could be adjusted to balance transmission and DEA degradation. Compared to the present work, the transmission ratio could be moderately increased for reducing actuation strain and improving system endurance. We estimate that a system level redesign can lead to 2 – 5 times improvement of flight time. In the longer term, lifetime improvement will be driven by new materials and processes. From the perspective of flexural materials, future works may incorporate nitinol (58) and polymer (59) hinges in the SCM system because these materials have shown high fatigue limit. From the perspective of DEA fabrication, other electrode materials such as graphene and silver nanowire may be explored because they have higher conductivity and produce less heat.

This robot platform has the potential to enable follow up studies on control, sensing, and power autonomy (*35*). While this work did not demonstrate heading angle control, it could be achieved by tilting each robot module during assembly (*16, 36*). Owing to its consistency and long lifespan, this robot can be used to evaluate other planning frameworks such as model predicative control (MPC) or reinforcement learning (RL). These planning methods can enable aggressive maneuvers such as banked turns and perching. More broadly, this robot is a fitting platform for exploring sensing and power autonomy – some of the most challenging directions for insect-scale MAVs. This robot has over 500 mg of payload capacity, which is sufficient for carrying a sensor suite including gyroscopes, accelerometers, and small cameras. There still exists a moderate gap for this robot to achieve power autonomy. The DEA consumes 2.9 W of reactive power ($\frac{1}{2}CV^2f$) during hovering flight, where C is the total DEA capacitance, V is the applied voltage, and f is the flapping-wing frequency. At this scale, it is difficult for sub-gram circuits and batteries to deliver the required power and voltage. Towards enabling power autonomous flight, future studies should focus on improving robot aerodynamic efficiency and payload capacity.

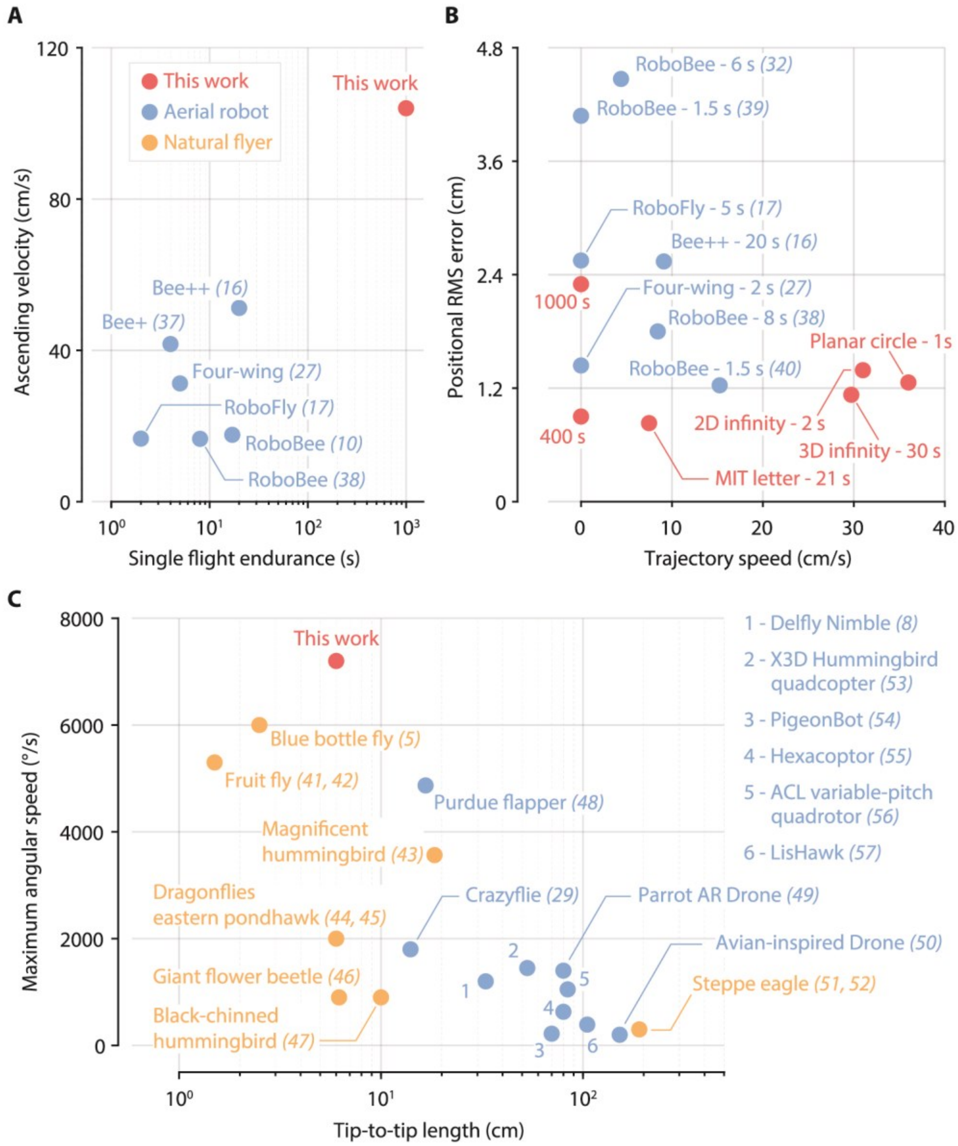

Fig. 7. Comparison of MAV flight performance. (**A**) Flight time and maximum ascending speed of existing sub-gram MAVs. (**B**) MAV mean flight speed and RMS position error during trajectory following flight. (**C**) Maximum angular rotational rate as a function of vehicle length scale. The blue and orange dots represent MAV and insect performance, respectively.

MATERIALS AND METHODS

1. Fabrication of robot components

The robot airframe, transmissions, connecting bars, and wings are made through the SCM process. The airframe is made of 160 μm carbon fiber, which consists of orthogonally stacked M55J laminates.

The airframe has 12 parts that are hand assembled into one structure (fig. S1A). This design has six I-beams for reinforcing structural strength and reducing oscillation during actuation.

The robot wing and wing hinge are combined into a single structure (Fig. 1C). There are seven material layers in the laminate fabrication process (fig. S1B). The top five layers consist of carbon fiber (70 μm), adhesive (12 μm), polyimide (25 μm), adhesive (12 μm), and carbon fiber (70 μm), which function as the compliant flexure. The bottom 2 layers consist of adhesive (12 μm) and polyester (1.5 μm), which act as the wing. By combining the wing and wing hinge into one structure, this design removes the prior mating feature (*21*) and improves the component alignment and consistency. Compared to prior designs (Fig. 3A), the wing shape is adjusted to accommodate the long hinge along the wing leading edge, and the wing area is increased by 2 times. The wingspan (R), aspect ratio (AR), first ($\hat{r}_1$), and second radius moment ($\hat{r}_2$) are 1.4 cm, 3, 0.49, and 0.55, respectively. Based on a blade element quasi-steady model (*60*), the distance between the wing root and the wing spanwise COP is given by: $R_{cop} = R\frac{\hat{r}_2^2}{\hat{r}_1} = 8.68$ mm.

The robot transmission consists of three sets of linear four bar mechanisms. The central transmission (fig. S1C) has a width and length of 0.8 mm and 1.8 mm, respectively. Compared to prior works (*30*), the transmission stiffness increases by 50% and the transmission ratio decreases by 52%. These changes of transmission design aim to increase the system resonance frequency and reduce the wing stroke amplitude. To mitigate off-axis bending, two guide transmissions were placed orthogonal to the main transmission (fig. S1C). The transmission stiffness of the guide transmissions is approximately 10% that of the main transmission, which implies they have small influence on system resonance and operating conditions.

The DEA is made using an existing fabrication method (*30*). We redesigned the DEA geometry to accommodate the new transmission and wing design. Compared to the prior designs (*21, 30*), the DEA length is reduced from 9 mm to 5 mm, and the number of electrode layers increases from 6 to 10. The electrode layer consists of single-wall carbon nanotube (SWCNT, Invisicon 3500, Nano-C Inc) that is less than 30 nm thick. The elastomeric layer thickness is 36 μm, which is identical to that in a prior work *(30).* The new DEA weighs 110 mg, and it is shown in fig. S1D. Compared to prior designs, this new DEA shows approximately two times increase of resonance frequency and blocked force but it has a two times reduction of displacement. This new design is advantageous because its short geometry mitigates nonlinear buckling (*21*). The robot is driven by four independent DEAs each requiring a high voltage line and a ground line. We designed two connector plates (fig. S1E) for the DEAs that shared the same ground line. This central connector plate design reduces the number of wires and mitigates wire-induced torques during flight. Supplementary Discussion S1 describes the selection process of the robot design parameters, which is documented in Table S1.

2. Experimental setup for static characterization and flight experiments

We conducted static and free flight experiments to characterize robot performance. In this work, we set up static flapping, constrained liftoff, constrained rotation, and free flight experiments. Fig. S2A shows an image of the static flapping set up. The robot is affixed in front of a high-speed camera (Phantom VEO 710) and it is illuminated by a halogen light (Amscope HL150-A). A custom control computer (Speedgoat) sends the command signal into a high voltage amplifier (Trek 677B), which drives the DEA in the range of 200 – 500 Hz and 1200 – 2000 V. The flapping-wing motion is recorded at 22000 frames per second (fps). The recorded high-speed videos are processed manually to extract instantaneous flapping-wing kinematics (Fig. 2D). To extract the stroke amplitudes for multiple experiments (Fig. 2E), we modified an automated tracking method based on a prior work (*21*).

After conducting the static flapping experiments, we drove the robot again under the same operating conditions while mounting it on a liftoff stand (fig. S2B). The liftoff stand consists of a beam that is balanced around a pivot. If the robot generates higher force than its weight, it ascends upward. To precisely measure the average lift force, we placed different payloads on either side of the balance beam under different operating conditions. The liftoff process is recorded by the high-speed camera at 3000 fps, and then the liftoff angle is extracted through an automated algorithm (*28*). The net lift force is calculated based on the tracked beam angle. The set of liftoff tests determine the optimal operating frequency and the voltage to force mapping in free flight experiments.

In preparation for body flip demonstrations, we conducted constrained rotation experiments (Fig. 2C). Fig. S2C shows an image of the setup where one robot module is mounted around a beam. To accurately estimate robot rotational speed in free flight experiments, the distance from the robot module to the rotation center is set to half of the robot connector length (Fig. 1B). The rotation center is approximately at the same location as the robot center of mass during free flight. We operated the robot at 1800 V and 330 Hz (movie S1 part 3 and Fig. 3C), and we recorded the high-speed video at 3000 fps. We manually tracked the beam angle (fig. S2I) and found the maximum rotational speed and average acceleration to be 9700 $°s^{-1}$ and 46200 $°s^{-2}$. This experiment demonstrates our robot can generate large body torque and achieve large rotational speed.

We conducted a sequence of hovering (Fig. 4, fig. S3), trajectory tracking (Fig. 5, fig. S4-7), and body flip (Fig. 6, fig. S8-10) experiments to demonstrate robot flight capabilities. The experiments were performed in an existing flight arena (*30*) (fig. S3A). The flight arena is equipped with a motion capture system, custom Simulink-Realtime control hardware and high voltage amplifiers. In addition to using the same high-speed camera in previous parts, we also used a color camera (Sony FX3) for recording flight (fig. S3A). To ensure continuous tracking during the fast body flips, seven 1.5 mm reflective markers were mounted on both sides of the robot to improve tracking robustness. Five markers were placed on the robot's upward facing side, and two markers were placed on the bottom side. These seven markers have a net weight of 40 mg, which is 10% of the estimated net payload. The motion capture system returns tracked position and orientation data. To calculate velocity and rotational speed, we processed the data with a lowpass filter before taking numerical derivatives. The controller runs at 2 kHz and commands the amplifiers at 10 kHz. The robot has four independently controlled DEAs, and it is tethered to the amplifiers through 49-gauge quadruple-insulated wires (MWS).

Supplementary Materials
Supplementary Discussion S1 to S5
Figs. S1 to S10
Table S1
Captions for Movies S1 to S10
Movies S1 to S10

References (*61–62*)

References and Notes

1. G. Card, M. H. Dickinson, Visually mediated motor planning in the escape response of Drosophila. *Current Biology* **18**, 1300-1307 (2008).
2. Z. J. Wang, J. Melfi Jr, A. Leonardo, Recovery mechanisms in the dragonfly righting reflex. *Science* **376**, 754-758 (2022).
3. P. Henningsson, L. Johansson, Downstroke and upstroke conflict during banked turns in butterflies. *Journal of the Royal Society Interface* **18**, 20210779 (2021).
4. J. A. Bender, M. H. Dickinson, Visual stimulation of saccades in magnetically tethered Drosophila. *Journal of Experimental Biology* **209**, 3170-3182 (2006).
5. P. Liu, S. P. Sane, J.-M. Mongeau, J. Zhao, B. Cheng, Flies land upside down on a ceiling using rapid visually mediated rotational maneuvers. *Science Advances* **5**, eaax1877 (2019).
6. J. M. Melis, I. Siwanowicz, M. H. Dickinson, Machine learning reveals the control mechanics of the insect wing hinge. *bioRxiv*, 2023.2006. 2029.547116 (2023).
7. W. Salem, B. Cellini, H. Kabutz, H. K. Hari Prasad, B. Cheng, K. Jayaram, J. M. Mongeau, Flies trade off stability and performance via adaptive compensation to wing damage. *Science Advances* **8**, eabo0719 (2022).
8. M. Karásek, F. T. Muijres, C. De Wagter, B. D. Remes, G. C. de Croon, A tailless aerial robotic flapper reveals that flies use torque coupling in rapid banked turns. *Science* **361**, 1089-1094 (2018).
9. Z. Tu, F. Fei, J. Zhang, X. Deng, An at-scale tailless flapping-wing hummingbird robot. I. design, optimization, and experimental validation. *IEEE Transactions on Robotics* **36**, 1511-1525 (2020).
10. K. Y. Ma, P. Chirarattananon, S. B. Fuller, R. J. Wood, Controlled flight of a biologically inspired, insect-scale robot. *Science* **340**, 603-607 (2013).
11. L. Hines, D. Campolo, M. Sitti, Liftoff of a motor-driven, flapping-wing microaerial vehicle capable of resonance. *IEEE Transactions on Robotics* **30**, 220-232 (2013).
12. D. S. Drew, N. O. Lambert, C. B. Schindler, K. S. Pister, Toward controlled flight of the ionocraft: a flying microrobot using electrohydrodynamic thrust with onboard sensing and no moving parts. *IEEE Robotics and Automation Letters* **3**, 2807-2813 (2018).
13. H. V. Phan, H. C. Park, Mechanisms of collision recovery in flying beetles and flapping-wing robots. *Science* **370**, 1214-1219 (2020).
14. Y.-W. Chin, J. M. Kok, Y.-Q. Zhu, W.-L. Chan, J. S. Chahl, B. C. Khoo, G.-K. Lau, Efficient flapping wing drone arrests high-speed flight using post-stall soaring. *Science Robotics* **5**, eaba2386 (2020).
15. R. J. Wood, E. Steltz, R. Fearing, Optimal energy density piezoelectric bending actuators. *Sensors and Actuators A: Physical* **119**, 476-488 (2005).
16. R. M. Bena, X. Yang, A. A. Calderón, N. O. Pérez-Arancibia, High-performance six-DOF flight control of the Bee++: an inclined-stroke-plane approach. *IEEE Transactions on Robotics* **39**, 1668-1684 (2023).
17. Y. M. Chukewad, J. James, A. Singh, S. Fuller, RoboFly: An insect-sized robot with simplified fabrication that is capable of flight, ground, and water surface locomotion. *IEEE Transactions on Robotics* **37**, 2025-2040 (2021).
18. T. Ozaki, N. Ohta, T. Jimbo, K. Hamaguchi, A wireless radiofrequency-powered insect-scale flapping-wing aerial vehicle. *Nature Electronics* **4**, 845-852 (2021).
19. M. A. Graule, P. Chirarattananon, S. B. Fuller, N. T. Jafferis, K. Y. Ma, M. Spenko, R. Kornbluh, R. J. Wood, Perching and takeoff of a robotic insect on overhangs using switchable electrostatic adhesion. *Science* **352**, 978-982 (2016).
20. Y. Chen, H. Wang, E. F. Helbling, N. T. Jafferis, R. Zufferey, A. Ong, K. Ma, N. Gravish, P. Chirarattananon, M. Kovac, R. J. Wood, A biologically inspired, flapping-wing, hybrid aerial-aquatic microrobot. *Science Robotics* **2**, eaao5619 (2017).

21. Y. Chen, H. Zhao, J. Mao, P. Chirarattananon, E. F. Helbling, N. S. P. Hyun, D. R. Clarke, R. J. Wood, Controlled flight of a microrobot powered by soft artificial muscles. *Nature* **575**, 324-329 (2019).
22. S. Kim, Y.-H. Hsiao, Y. Lee, W. Zhu, Z. Ren, F. Niroui, Y. Chen, Laser-assisted failure recovery for dielectric elastomer actuators in aerial robots. *Science Robotics* **8**, eadf4278 (2023).
23. Y.-H. Hsiao, S. Kim, S. Ceron, Z. Ren, Y. Chen, Modular and Scalable Fabrication of Insect-Scale Aerial Robots toward Demonstrating Swarm Flights. *Advanced Intelligent Systems* **6**, 2300059 (2024).
24. J. P. Whitney, P. S. Sreetharan, K. Y. Ma, R. J. Wood, Pop-up book MEMS. *Journal of Micromechanics and Microengineering* **21**, 115021 (2011).
25. E. Appel, J. Michels, S. N. Gorb, Resilin in insect flight systems. *Advanced Functional Materials*, 2215162 (2023).
26. O. Kraft, R. Schwaiger, P. Wellner, Fatigue in thin films: lifetime and damage formation. *Materials Science and Engineering: A* **319**, 919-923 (2001).
27. S. B. Fuller, Four wings: an insect-sized aerial robot with steering ability and payload capacity for autonomy. *IEEE Robotics and Automation Letters* **4**, 570-577 (2019).
28. Y. Chen, S. Xu, Z. Ren, P. Chirarattananon, Collision resilient insect-scale soft-actuated aerial robots with high agility. *IEEE Transactions on Robotics* **37**, 1752-1764 (2021).
29. Y. Chen, N. O. Pérez-Arancibia, Controller synthesis and performance optimization for aerobatic quadrotor flight. *IEEE Transactions on Control Systems Technology* **28**, 2204-2219 (2019).
30. Z. Ren, S. Kim, X. Ji, W. Zhu, F. Niroui, J. Kong, Y. Chen, A high-lift micro-aerial-robot powered by low-voltage and long-endurance dielectric elastomer actuators. *Advanced Materials* **34**, 2106757 (2022).
31. Y. Chen, K. Ma, R. J. Wood, Influence of wing morphological and inertial parameters on flapping flight performance, in *2016 IEEE/RSJ International Conference on Intelligent Robots and Systems (IROS)*, pp. 2329-2336 (2016).
32. R. McGill, N.-S. P. Hyun, R. J. Wood, Modeling and control of flapping-wing micro-aerial vehicles with harmonic sinusoids. *IEEE Robotics and Automation Letters* **7**, 746-753 (2021).
33. P. Sareh, P. Chermprayong, M. Emmanuelli, H. Nadeem, M. Kovac, Rotorigami: A rotary origami protective system for robotic rotorcraft. *Science Robotics* **3** (2018).
34. T. Helps, C. Romero, M. Taghavi, A. T. Conn, J. Rossiter, Liquid-amplified zipping actuators for micro-air vehicles with transmission-free flapping. *Science Robotics* **7**, eabi8189 (2022).
35. E. F. Helbling, R. J. Wood, A review of propulsion, power, and control architectures for insect-scale flapping-wing vehicles. *Applied Mechanics Reviews* **70**, p.010801 (2018).
36. Y.-H. Hsiao, S. Kim, Z. Ren, Y. Chen, Heading control of a long-endurance insect-scale aerial robot powered by soft artificial muscles, in *2023 IEEE International Conference on Robotics and Automation (ICRA)*, pp. 3376-3382 (2023).
37. X. Yang, Y. Chen, L. Chang, A.A. Calderon, N.O. Perez-Arancibia, Bee+: A 95-mg four-winged insect-scale flying robot driven by twinned unimorph actuators. *IEEE Robotics and Automation Letters* **4**, 4270-4277 (2019).
38. P. Chirarattananon, K. Y. Ma, and R. J. Wood, Adaptive control of a millimeter-scale flapping-wing robot. *Bioinspiration & Biomimetics* **9**, 025004 (2014).
39. A. De, R. McGill, and R. J. Wood, An efficient, modular controller for flapping flight composing model-based and model-free components. *The International Journal of Robotics Research* **41**, 441-457 (2022).
40. P. Chirarattananon, K. Y. Ma, and R. J. Wood, Single-loop control and trajectory following of a flapping-wing microrobot, in *2014 IEEE International Conference on Robotics and Automation (ICRA)* (2014).
41. F. T. Muijres, M. J. Elzinga, J. M. Melis, M. H. Dickinson, Flies evade looming targets by executing rapid visually directed banked turns. *Science* **344**, 172-177 (2014).

42. A. Susanto, S. Sudarjat, E. Yulia, A. D. Permana, A. Gunawan, D. H. Yudistira, Effectiveness of modified traps for protection against fruit flies on mango. *Jurnal Biodjati* **5**, 99-106 (2020).

43. B. Cheng, B. W. Tobalske, D. R. Powers, T. L. Hedrick, Y. Wang, S. M. Wethington, G. T. Chiu, X. Deng, Flight mechanics and control of escape manoeuvres in hummingbirds. II. Aerodynamic force production, flight control and performance limitations. *Journal of Experimental Biology* **219**, 3532-3543 (2016).

44. S. Zeyghami, H. Dong, Study of turning takeoff maneuver in free-flying dragonflies: effect of dynamic coupling, arXiv preprint arXiv:1502.06858 (2015).

45. C. Li, H. Dong, Wing kinematics measurement and aerodynamics of a dragonfly in turning flight. *Bioinspiration & Biomimetics* **12**, 026001 (2017).

46. Y. Li, F. Cao, T. T. V. Doan, H. Sato, Controlled banked turns in coleopteran flight measured by a miniature wireless inertial measurement unit. *Bioinspiration & Biomimetics* **11**, 056018 (2016).

47. W. H. Baltosser, S. M. Russell, Black-chinned Hummingbird (Archilochus alexandri). *The birds of North America* **495**, 32 (2000).

48. Z. Tu, F. Fei, X. Deng, Bio-inspired rapid escape and tight body flip on an at-scale flapping wing hummingbird robot via reinforcement learning. *IEEE Transactions on Robotics* **37**, 1742-1751 (2021).

49. F. Oliva-Palomo, A. Sanchez-Orta, P. Castillo, H. Alazki, Nonlinear ellipsoid based attitude control for aggressive trajectories in a quadrotor: Closed-loop multi-flips implementation. *Control Engineering Practice* **77**, 150-161 (2018).

50. E. Ajanic, M. Feroskhan, V. Wüest, D. Floreano, Sharp turning maneuvers with avian-inspired wing and tail morphing. *Communications Engineering* **1**, 34 (2022).

51. G. Taylor, M. Bacic, A. Carruthers, J. Gillies, Y. Ozawa, A. Thomas, Flight control mechanisms in birds of prey, in *45th AIAA Aerospace Sciences Meeting and Exhibit*, pp. 39, (2007).

52. B.-U. Meyburg, P. Paillat, C. Meyburg, Migration routes of Steppe Eagles between Asia and Africa: a study by means of satellite telemetry. *The Condor* **105**, 219-227 (2003).

53. S. Lupashin, A. Schöllig, M. Sherback, R. D'Andrea, A simple learning strategy for high-speed quadrocopter multi-flips, in *2010 IEEE International Conference on Robotics and Automation*, pp. 1642-1648 (2010).

54. E. Chang, L. Y. Matloff, A. K. Stowers, D. Lentink, Soft biohybrid morphing wings with feathers underactuated by wrist and finger motion. *Science Robotics* **5**, eaay1246 (2020).

55. A. Tagliabue, J. P. How, Efficient deep learning of robust policies from MPC using imitation and tube-guided data augmentation, arXiv preprint arXiv:2306.00286 (2023).

56. M. Cutler, J. P. How, Analysis and control of a variable-pitch quadrotor for agile flight. *Journal of Dynamic Systems, Measurement, and Control* **137**, 101002 (2015).

57. E. Ajanic, M. Feroskhan, S. Mintchev, F. Noca, D. Floreano, Bioinspired wing and tail morphing extends drone flight capabilities. *Science Robotics* **5**, eabc2897 (2020).

58. R.A. York, and R.J. Wood, Nitinol living hinges for millimeter-sized robots and medical devices. in *International Conference on Robotics and Automation,* pp. 889-893 (2019).

59. M.H. Rosen, G. Le Pivain, R. Sahai, N.T. Jafferis, and R.J. Wood, Development of a 3.2 g untethered flapping-wing platform for flight energetics and control experiments. in *IEEE international conference on robotics and automation,* pp. 3227-3233 (2016).

60. J.P. Whitney, and R.J. Wood, Aeromechanics of passive rotation in flapping flight. *Journal of fluid mechanics*, 660, 197-220 (2010).

61. H. Zhao, A. M. Hussain, M. Duduta, D. M. Vogt, R. J. Wood, D. R. Clarke, Compact dielectric elastomer linear actuators, *Advanced Functional Materials* **28**, 1804328 (2018).

62. Y. Chen, N. Gravish, A. L. Desbiens, R. Malka, R. J. Wood, Experimental and computational studies of the aerodynamic performance of a flapping and passively rotating insect wing, *Journal of Fluid Mechanics* **791**, 1-33 (2016).

Acknowledgments:
The authors thank Q. Kieu for discussion and help with image processing.

Funding:
National Science Foundation grant 2202477, 2236708 (YC)
Mathworks Fellowship (YH)

Author contributions:

Conceptualization: SK, YH, YC
Methodology: SK, YH, YC
Software: YH, SK, ZR, JH, YC
Validation: YH, SK, ZR, JH, YC
Formal analysis: YH, SK, ZR, JH, YC
Investigation: SK, YH, YC
Resources: YC
Data curation: SK, YH, YC
Writing – Original draft: SK, YH, YC
Writing – Review & editing: YH, SK, ZR, JH, YC
Visualization: YH, SK, ZR, JH, YC
Supervision: YC
Project administration: YC
Funding acquisition: YC

Competing interests: Authors declare that they have no competing interests.

Data and materials availability: The flight data is available in the data repository Dryad with DOI: https://doi.org/10.5061/dryad.0p2ngf28q. The reviewers can use this link provided by Dryad: https://datadryad.org/stash/share/WdnrDpF-kbItUEEgK1-mzQD5uT-Fh1hnP-aZ-DHosmY.